Control of ice thickness in cryo-EM via confinement

Liming Zheng[†1,3], Jiling Song[†2], Xiaole Zhao[†1], Jiacong Cao[4], Jie Xu[2], Zhengni Wang[2], Chenhui Zhang[5], Weiyu Sun[1,6], Buhang Chen[7], Xiaoyin Gao[1], Haonan Liu[8], Junhao Yang[2], Yu Xu[9,10], Luzhao Sun[7], Zhaohe Dai[4], Xiaoding Wei[4], Nan Liu[*5], Hailin Peng[*1,6], Hong-Wei Wang[*2]

[1] Beijing National Laboratory for Molecular Sciences, *College of Chemistry and Molecular Engineering, Peking University, Beijing 100871, China.*

[2] *Ministry of Education Key Laboratory of Protein Sciences, Beijing Frontier Research Center for Biological Structures, Tsinghua-Peking Joint Center for Life Sciences, School of Life Sciences, Tsinghua University, Beijing 100084, China.*

[3]*Institute for Functional Intelligent Materials, National University of Singapore, Singapore, Singapore*

[4] *State Key Laboratory for Turbulence and Complex System, Department of Mechanics and Engineering Science, College of Engineering, Peking University, Beijing 100871, China.*

[5] *School of Biological Sciences, The University of Hong Kong, Hong Kong, 999077, China.*

[6] *Academy for Advanced Interdisciplinary Studies, Peking University, Beijing 100871, China.*

[7] *Beijing Graphene Institute (BGI), Beijing 100095, China.*

[8] *Key Laboratory for the Physics and Chemistry of Nanodevices and Center for Carbon-based Electronics, School of Electronics, Peking University, Beijing 100871, China*

[9] *Tsinghua Shenzhen International Graduate School, Tsinghua University, Shenzhen 518055, Guangdong, China.*

[10] *Institute of Bio-Architecture and Bio-Interactions, Shenzhen Medical Academy of Research and Translation, Shenzhen 518107, Guangdong, China.*

*Correspondence should be addressed to H.W., H.P., or N.L.

(e-mail: hongweiwang@tsinghua.edu.cn, hlpeng@pku.edu.cn, nanliu@hku.hk)

† These authors contributed equally to this work.

Abstract

Achieving thin ice with optimal thickness is a prerequisite for successful cryo-EM analysis of embedded macromolecules. Despite decades of effort, precise control of ice thickness in cryo-EM remains a major challenge. Here, we reveal that the intrinsic instability of sub-100-nm liquid film, a previously overlooked determinant prior to vitrification, plays a critical role in controlling ice thickness. We found that well-designed graphene reservoirs can confine liquid film to an optimal thickness and overcome the limitations posed by liquid film instability, achieving precise control of ice thickness with robust reproducibility and large-area uniformity. These graphene reservoirs demonstrate superior liquid retention capabilities than conventional techniques, enabling tunable ice thickness through reservoir depth modulation. Moreover, this approach yields uniform confined ice in graphene sandwiches with controllable thickness and high efficiency, facilitating cryo-EM imaging of a broad range of macromolecule particles with high contrast, reduced motion and diverse orientations for more robust high-resolution reconstruction.

Cryo-electron microscopy (cryo-EM) has expanded beyond structural biology into cross-disciplinary domains[1], driving breakthroughs in drug discovery[2,3], battery design[4,5], and materials innovation[6,7]. In cryo-EM, target samples are embedded in vitreous ice, whose thickness critically dominates the success of cryo-EM analysis because it directly governs the imaging background noise, sample distribution, and the attainable resolution of reconstructed structure[8-10]. However, despite decades of continuous efforts, the control of ice thickness remains unattainable[11,12]. Current techniques for ice preparation suffer from poor reproducibility and heterogeneous ice thickness, rendering the thickness control predominantly a trial-and-error process[13-15]. Given that the vitreous ice is formed by rapid cooling of a thin liquid film, the bottleneck likely lies in the thin liquid film itself, necessitating investigation into the thermodynamic constraints that govern liquid film formation.

Theoretical calculations showed that when a liquid film is thinner than a critical threshold of ~100 nm, a thickness desired for high-resolution cryo-EM imaging, it becomes unstable and undergoes spontaneous thinning[16,17]. This process is driven by molecular migration from thinner regions to adjacent thicker areas, where their van der Waals (vdW) energy is more favorable. The energy-driven migration causes the thin liquid film to rupture easily and break into microscopic droplets[18], a process that is profound yet unpredictable. This intrinsic instability of sub-100-nm liquid film fundamentally constrains both the uniformity and reproducibility of vitreous ice formation in cryo-EM.

Recently, liquid under confinement has attracted wide interest due to its emergent physical properties[19,20]. The confined liquid exhibits significantly slowed molecular migration and a suppressed diffusion coefficient that can be 2-8 orders of magnitude smaller than in bulk[21-23]. Moreover, the confinement structures can spatially mold the liquid film, even when its thickness is reduced to several atomic layers[24,25]. These findings suggest that confinement may overcome

the thermodynamic limit in preparing sub-100-nm thin liquid film, providing a key to reliable ice formation for high-resolution cryo-EM imaging. The confinement strategy also aligns with the long-pursued goal of sandwiching samples between thin membranes[12,18], in which graphene is a promising membrane for liquid encapsulation due to its atomic thickness, excellent flexibility and high conductivity. Unfortunately, the thin liquid film within graphene sandwich encountered the same challenge. Both reproducibility and uniformity are poorly controlled due to the lack of effective control of confinement architectures[26,27].

In this work, we have investigated the liquid confinement in reservoirs made of graphene over perforated supporting films, realizing the precise control of ice thickness by adjusting the dimensions and edge profiles of the holes (Fig. 1a). These graphene reservoirs feature a characteristic sagging morphology with controllable depths reaching tens of nanometers. Compared with previously established techniques, the graphene reservoirs demonstrate exceptional liquid retention capabilities, even under extreme specimen preparation conditions. By adjusting the graphene reservoir depth, we can achieve precise control of vitreous ice thickness with both large-area uniformity and excellent reproducibility. Notably, this approach also enables efficient thickness regulation of confined ice in graphene sandwich configurations (Fig. 1b), overcoming a long-standing challenge that has limited their widespread application in biological and chemical research. The graphene reservoir and derived graphene reservoir sandwich techniques demonstrated high reproducibility in preparing high-quality cryo-EM specimens across diverse macromolecules in our studies, ranging from protein to RNA molecules, enabling high-resolution structural determination.

Design and depth control of graphene reservoirs

Unlike bulk materials, atomically thin graphene over a hole is prone to adhere to the hole sidewalls due to vdW attraction[20], and this adhesion causes graphene sagging (Fig. 1). Previous measurements showed that the sagging depth of graphene over holes (diameter ~1 μm) ranged from 2 nm to 30 nm[28-30], primarily determined by the uneven hole edge morphology and vdW interaction strength[31]. To achieve uniform sagging depth, we employed an industry-compatible lithography technique for precise control of hole edge morphology. This technique enabled the fabrication of hole arrays on a 6-inch wafer (Fig. 2a) at a high density of ~2.9×10^9 holes per wafer (Methods). Benefiting from the nanoscale precision of lithography, the resulting holes are identical and exhibit smooth rounded edges (Fig. 2b, Fig. S1), a desired morphology that facilitates the sagging of suspended graphene[31]. Using these holes as template, we achieved scalable fabrication of home-made EM grids (Figs. S2, S3). The EM grids enabled the high-coverage and clean transfer of graphene, with the suspended graphene sagging into the holes to form what we term graphene reservoirs (Fig. 2c, Fig. S4).

Atomic force microscopy (AFM) revealed that graphene membranes of graphene reservoirs were stretched tautly across the hole edges, and the sagging depth was ~30 nm in 1200-nm diameter holes (Fig. 2d). Statistical analysis further confirmed the uniformity of sagging depth (Fig. 2e),

demonstrating the effectiveness of our design on hole morphology for reliable graphene reservoir formation. By varying the hole diameter from 600 nm to 2000 nm, we achieved controllable graphene sagging depths of ~14 nm, ~22 nm, ~30 nm, and ~40 nm, respectively (Fig. 2f, Fig.S5). These experiment results were supported by our theoretical model (Fig. S6, Supporting Information). In this model, the competition between vdW potential and stretching energy of graphene decides the sagging depth. By balancing the vdW potential and stretching energy, the sagging depth w_0 can be described by

$$w_0 = kD^{\frac{2}{5}} R_c^{\frac{3}{5}} \Gamma^{\frac{2}{5}} E_{2D}^{-\frac{2}{5}} \qquad \text{Eq. (1)}$$

where k is a constant, D is the hole diameter, R_c is the curvature radius of the hole edge, Γ represents the adhesion energy between graphene and hole edge, and E_{2D} is the Young's modulus of graphene, respectively. Therefore, increasing the hole diameter (D) and enlarging the curvature radius (R_c) of hole edges—which corresponds to smoother edge morphology—contribute to enhanced sagging depth w_0 (Fig. 2f). In contrast, conventional commercially available EM grids often have a sharply protruding hole edge[32], when transferred with graphene membranes, leading to the outward bulging of graphene membranes on the holes (Fig. 2g, Fig. S7). The bulging height reaches up to ~45 nm (Fig. 2h), which poses challenges for controlling ice thickness, as discussed subsequently.

Precise control of ice thickness in cryo-EM

The sagging morphology of graphene reservoirs, naturally creating localized containers, inspired us to investigate their liquid preservation capabilities. To test this, we employed the standard blotting method to our graphene reservoir-equipped grids (1200-nm diameter holes) for ice layer preparation. As shown in Figure 3a, excess liquid was wicked away from graphene reservoir surface using filter paper to form a confined liquid film for subsequent ice formation. Cryo-electron tomography (cryo-ET) revealed that this confined liquid film indeed exhibited a sagging morphology within the graphene reservoir (Fig. S8). Surprisingly, we found that the confined liquid film remained stable even after a significantly extended blotting time of 10 seconds, which is 5–10 times longer than typical blotting durations in our usual practice (usually 1–2 s) on conventional graphene grid. Protein particles were well-dispersed in such vitrified liquid film and preserved their native structures (Fig. 3a, lower panel). The proteins' three-dimensional (3D) spatial distributions within the vitreous ice were resolved using single-particle analysis (Fig. 3b) and cryo-ET (Fig. 3c). As showed by the results, most protein particles were adsorbed at the graphene-water interface or distributed in the ice layer (Fig. 3b-c), away from the detrimental air-water interface which is known to cause protein denaturation and preferential orientation[12,33,34]. Both single-particle analysis and cryo-ET measurements revealed a consistent ice thickness of ~30 nm (Fig. 3b-c, Fig. S9), closely matching the sagging depth of the graphene reservoir (Fig. 2d-e), revealing the graphene reservoir's capability for ice thickness control.

We further evaluated the reproducibility and large-area uniformity of ice thickness prepared with graphene reservoirs. We used cryo-ET reconstruction to measure the ice thickness across different regions of multiple specimens prepared with varying blotting times. The average ice thickness was 119 ± 9 nm, 52 ± 9 nm, 33 ± 7 nm, 28 ± 3 nm, and 27 ± 2 nm for blotting time of 2 s, 6 s, 8 s, 10 s, and 12 s, respectively (blue data, Fig. 3d, Fig. S10). Independent replicate experiments under identical conditions produced comparable results (106 ± 11 nm, 49 ± 6 nm, 35 ± 7 nm, 27 ± 3 nm, and 27 ± 3 nm; green data, Fig. 3d, Fig. S11), demonstrating the reliability of graphene reservoirs in controlling ice thickness. Notably, extending the blotting time beyond 10 seconds led to a plateau in ice thickness at 27 ± 3 nm. This means the graphene reservoir design provides a robust platform for reproducible thin ice preparation. Besides, the confined ice layer exhibited uniform ice thickness across the entire grid, as revealed by the overview atlas of the grid with homogeneous brightness and unnoticeable variability (Fig. 3e).

We then explored if the plateau thickness of ice can be tailored by adjusting the sagging depths of graphene reservoirs. To create reservoirs with varying depths, we first fabricated holey foils with diameters ranging from 600 nm to 2000 nm. After graphene coating, these structures produced reservoirs with different depths, as previously demonstrated (Fig. 2f). Indeed, controllable ice thicknesses of ~15 nm, ~20 nm, ~30 nm, and ~40 nm were achieved using graphene reservoirs with corresponding hole diameters (Fig. 3f, Fig. S12). The measured ice thickness closely matched the sagging depths of their respective graphene reservoirs (Fig. 2f), further confirming our confinement approach for reliable ice thickness control. In contrast, the conventional grid (1200 nm diameter) with protruding holes suffered from rupture of the liquid film under the same blot time of 10 s (Fig. S13a-b). The ruptured liquid film and resultant uneven ice caused the protein aggregation and denaturation, leading to a significant reduction of usable particle percentage for cryo-EM reconstruction (Fig. S13c-d). These differences originate from the thermodynamic behavior of a sub-100-nm liquid film. The free energy of such film exhibits positive correlation with the long-range contribution of vdW force (P), as described by[16]:

$$P(h) = \frac{\mathrm{A}}{12\pi h^2} \qquad \text{Eq. (2)}$$

where h is the thickness of liquid film and $\mathrm{A} > 0$ for a wetting liquid. According to this equation, thinner films experience a higher vdW force, prompting spontaneous liquid migration toward thicker areas to achieve energy minimization. This mechanism also explains how graphene reservoirs retain liquid under extreme blotting conditions: liquid spontaneously migrates from thin peripheral regions into the thicker graphene reservoir domains (Fig. 3a). To make it more visible, we performed theoretical simulations to reveal the diffusion behavior of liquid film around the graphene reservoirs. As shown in Figure 3g, liquid flow velocity in thin peripheral regions significantly exceeds that in thicker graphene reservoir areas, directly driving liquid influx into graphene reservoirs. This phenomenon consistently appears across graphene reservoirs with different sagging depths (Fig. S14). Conversely, conventional graphene grids exhibit inverse thickness profiles: protruding edges create thinner central films relative to peripheral regions. This

inverted gradient induces detrimental liquid migration toward thicker edges, causing liquid film rupture in the hole regions and compromising thickness control (Fig. S13).

Ice confinement in graphene reservoir sandwich

The successful ice thickness control of graphene reservoirs provides new opportunities for a more challenging case—achieving the precise control of ice thickness confined in graphene sandwich structures (Fig. 4a, top), a task that has garnered significant interest but has yet to be accomplished[11,26]. Conventional sandwiched liquid suffers from intrinsic randomness (Fig. 4b): the size and location of graphene sandwich are unpredictable[21]. In light of this, graphene reservoirs can provide three key advantages: uniform dimensions, periodic arrangements, and thermodynamically favorable liquid migration, collectively making the formation of sandwiched liquid more controllable. As expected, the obtained confined ice in graphene reservoir sandwich is uniform (Fig. 4a), exhibiting a more homogeneous electron transmission than that in conventional graphene sandwich (Fig. 4b). Moreover, the large-area uniformity of confined ice can be well reproduced, as confirmed by the overview atlases of multiple grids (Fig. 4c, Fig. S15). The robust reproducibility benefits from graphene reservoirs' excellent liquid retention capability during extended blotting time. Detailed step-by-step procedures have been provided in Methods section to enable experimental replication. Most procedures are compatible with commonly-used blotting method in cryo-EM specimen preparation, facilitating broad and immediate applicability.

We further analyzed the distribution of protein molecules within the confined ice by the graphene reservoir sandwich and measured the ice thickness using cryo-ET. As shown in Figures 4d and 4e, the 20S proteasome particles predominantly adsorbed at both top and bottom graphene surfaces. The measured ice thickness was ~30 nm (Fig. 4d), which was suitable for embedding proteins without introducing extra background signal. The thickness statistics further demonstrated the uniformity of confined ice, which exhibited a narrow distribution centered at 30 nm and matched the sagging depth of graphene reservoirs (Fig. 4f, Fig. S16). In contrast, conventional graphene sandwiched ice showed larger thickness (52 ± 17 nm) with a high degree of variability (Fig. 4f, Fig. S17). Such thickness variation represents a major limitation for the broad application of the conventional graphene sandwich technique, as excessively thin ice layers compromise protein structural integrity, while overly thick ice layers obscure protein particles in cryo-EM imaging. Moreover, we found that the thickness of confined ice in graphene reservoir sandwich could also be precisely controlled by varying the layer number of graphene reservoir. Increasing from a monolayer to a tri-layer causes a threefold increase in E_{2D} (Eq. (1)), which inversely reduces the ice thickness from 30 ± 1 nm to 19 ± 2 nm (Fig. S18). This thickness reduction by $3^{-2/5}$ times aligns closely with model predictions.

Beyond ice thickness control, graphene reservoirs can enhance the efficiency in fabricating confined ice in sandwich. Quantitative analysis revealed a success rate of over 90% across 2,219 grid squares using our graphene reservoirs, versus ~67% for conventional method (N = 1,973 squares; Fig. 4g, Fig. S19). This high efficiency (>90%) ensures successful encapsulation of

macromolecules, minimizes costly retrials, and enables high-throughput cryo-EM data collection. We further compared the particle motion in confined ice (from graphene reservoir sandwich) and conventional sandwiched ice. The particle motion is mainly caused by beam-induced ice bulking during imaging[35], which degrades image quality and impairs high-resolution information in cryo-EM. Particles in confined ice exhibited reduced motion amplitude and enhanced convergence compared to those in conventional sandwiched ice (Fig. 4h). Thus, our method improves both specimen preparation efficiency and ultimate image quality.

Uniform confined ice for high-resolution reconstruction

With precisely controlled thickness of confined ice, we successfully resolved structures of multiple macromolecules at near-atomic resolution (Supplementary Table 1). The RNA particles (Ll.LtrB Group II intron) exhibited high contrast and diverse orientations in the confined ice prepared by graphene reservoirs (Fig. 5a and inset), enabling a high-resolution 3D reconstruction at 2.7 Å (Fig. 5b, Figs. S20a, S21). The resulting map revealed distinct side chains with well-fitted atomic structures (Fig. 5c). Similarly, the SARS-CoV-2 spike protein particles encapsulated in graphene reservoir sandwiches also exhibited high signal-to-noise ratio (Fig. 5d). The particles were mono-dispersed and showed multiple orientations (Fig. 5d, inset). The final 3D reconstruction was obtained at a near-atomic resolution of 2.9 Å (Fig. 5e-f, Fig. S20b).

Many small proteins with molecular weight less than 100 kDa are often targets in drug discovery, but their cryo-EM reconstructions require a uniform thin ice to minimize the background noise given their low contrast in cryo-EM. Conventional sandwiched ice is too thick for the imaging of such small proteins, exemplified by the 52-kDa streptavidin, whose particle images in sandwiched ice were almost indistinguishable and could not yield meaningful 3D reconstruction (Fig. S22). In the graphene reservoir sandwiched ice, however, individual streptavidin particles were clearly visible with high signal-to-noise ratio under cryo-EM (Fig. 5g). Such a specimen easily yields a 3D reconstruction of streptavidin at 2.7 Å (Fig. 5h, Figs. S20c, S23), enabling the distinct identification of side chains of amino acid residues (Fig. 5i). The successful structural determination of streptavidin in this work reveals the great potential of precisely controlled confined ice in high-resolution cryo-EM by graphene reservoir sandwich.

Discussion

In conventional preparation of thin vitreous ice, the intrinsic instability of sub-100-nm liquid film significantly impedes the ice thickness control, due to the energy-driven spontaneous thinning prior to vitrification[16-18]. Remarkably, our graphene reservoir design inverts the paradigm. We demonstrated that careful design and fabrication of the perforated supporting film, with optimal hole dimensions and edge shapes, are crucial for creating graphene reservoirs with the appropriate sagging depth to retain the liquid film before vitrification. The spontaneous migration of liquid into graphene reservoirs ensures their exceptional liquid retention capacity even under extreme

blotting conditions, making them ideally suited for cryo-EM applications. Crucially, the preserved film thickness closely corresponds to the reservoir sagging depth. Benefiting from this, the long-pursued precise control of ice thickness in cryo-EM has been achieved by confining the liquid within graphene reservoirs with controllable depths. The obtained ice layers exhibit large-area uniformity and robust reproducibility.

Notably, the graphene reservoirs also enable the fabrication of uniform confined liquid in graphene sandwiches. The graphene sandwich technique has garnered significant attention across materials science, chemistry and biology[36,37]. However, its widespread adoption has been limited by challenges in controlling liquid thickness and uniformity. Our approach yields confined ice with much greater thickness homogeneity, higher efficiency, and better reproducibility compared to conventional techniques, thereby providing a key to addressing this critical limitation. Based on precisely controlled ice thickness, we have successfully determined the 3D atomic structures of various macromolecules, including sub-100-kDa small biomolecules encapsulated in graphene sandwiches.

Given that the preparation of confined liquid in graphene reservoirs is compatible with conventional blotting techniques, the new method offers a more easy-to-handle procedure for both cryo-EM specimen preparation and in-situ liquid-phase imaging[8,9,38,39]. Beyond electron microscopy, the ability to precisely manipulate confined ice or liquid provides a powerful tool for investigating their emergent properties related to various physical, chemical and biological processes[19,40]. Moreover, the understanding of sagging depth of suspended graphene can be extended to other two-dimensional materials, facilitating their applications in separation membranes, electronic devices, and high-performance sensors.

References

1 Nogales, E. & Mahamid, J. Bridging structural and cell biology with cryo-electron microscopy. *Nature* **628**, 47-56 (2024).

2 Kretsch, R. C. *et al.* Naturally ornate RNA-only complexes revealed by cryo-EM. *Nature*, **643**, 1135-1142 (2025).

3 Gilbert, M. A. G. *et al.* CryoET of β-amyloid and tau within postmortem Alzheimer's disease brain. *Nature* **631**, 913-919 (2024).

4 Li, Y. Z. *et al.* Atomic structure of sensitive battery materials and Interfaces revealed by cryo-electron microscopy. *Science* **358**, 506-510 (2017).

5 Yuan, X. T., Liu, B., Mecklenburg, M. & Li, Y. Z. Ultrafast deposition of faceted lithium polyhedra by outpacing SEI formation. *Nature* **620**, 86-91 (2023).

6 Choi, H. S. *et al.* Molecularly thin, two-dimensional all-organic perovskites. *Science* **384**, 60-66 (2024).

7 Tian, J. *et al.* High-resolution cryo-electron microscopy structure of block copolymer nanofibres with a crystalline core. *Nat. Mater.* **22**, 786-792 (2023).

8 Banari, A. *et al.* Advancing time-resolved structural biology: latest strategies in cryo-EM and X-ray crystallography. *Nat. Methods* **22**, 1420-1435 (2025).

9 Bhattacharjee, S. *et al.* Time resolution in cryo-EM using a PDMS-based microfluidic chip assembly and its application to the study of HflX-mediated ribosome recycling. *Cell* **187**, 782-796 (2024).

10 Zheng, L. M. *et al.* Uniform thin ice on ultraflat graphene for high-resolution cryo-EM. *Nat. Methods* **20**, 123-130 (2023).

11 Singh, A. Graphene sandwich for cryo-EM. *Nat Methods* **21**, 371-371 (2024).

12 Han, B. G., Avila-Sakar, A., Remis, J. & Glaeser, R. M. Challenges in making ideal cryo-EM samples. *Curr. Opin. Struc. Biol.* **81**, 102646 (2023).

13 Armstrong, M. *et al.* Microscale Fluid Behavior during Cryo-EM Sample Blotting. *Biophys. J.* **118**, 708-719 (2020).

14 Glaeser, R. M. Preparing Better Samples for Cryo–Electron Microscopy: Biochemical Challenges Do not End with Isolation and Purification. *Annu. Rev. Biochem.* **90,** 8.1-8.24 (2021).

15 Weissenberger, G., Henderikx, R. J. M. & Peters, P. J. Understanding the invisible hands of sample preparation for cryo-EM. *Nat. Methods* **18**, 463-471 (2021).

16 Wyart, F. B. & Daillant, J. Drying of Solids Wetted by Thin Liquid-Films. *Can. J. Phys.* **68**, 1084-1088 (1990).

17 Yaminsky, V. V., Ohnishi, S., Vogler, E. A. & Horn, R. G. Stability of Aqueous Films between Bubbles. Part 1. The Effect of Speed on Bubble Coalescence in Purified Water and Simple Electrolyte Solutions. *Langmuir* **26**, 8061-8074 (2010).

18 Glaeser, R. M. *et al.* Factors that Influence the Formation and Stability of Thin, Cryo-EM Specimens. *Biophys. J.* **110**, 749-755 (2016).

19 Fumagalli, L. *et al.* Anomalously low dielectric constant of confined water. *Science* **360**, 1339-1342 (2018).

20 Yang, Q. *et al.* Capillary condensation under atomic-scale confinement. *Nature* **588**, 250-253 (2020).

21 Zhang, D. Y., Xu, Z. P., Li, J. Y., Mao, S. & Wang, H. Graphene-Assisted Electron-Based Imaging of Individual Organic and Biological Macromolecules: Structure and Transient Dynamics. *ACS Nano* **19**, 120-151 (2024).

22 Zheng, H. M. *et al.* Observation of Single Colloidal Platinum Nanocrystal Growth Trajectories. *Science* **324**, 1309-1312 (2009).

23 Shin, D. H. *et al.* Growth dynamics and gas transport mechanism of nanobubbles in graphene liquid cells. *Nat. Commun.* **6**, 6068 (2015).

24 Esfandiar, A. *et al.* Size effect in ion transport through angstrom-scale slits. *Science* **358**, 511-513 (2017).

25 Gopinadhan, K. *et al.* Complete steric exclusion of ions and proton transport through confined monolayer water. *Science* **363**, 145-147 (2019).

26 Xu, J. *et al.* Graphene sandwich-based biological specimen preparation for cryo-EM analysis. *Proc. Natl. Acad. Sci. U.S.A.* **121**, e2309384121 (2024).

27 Zhang, D. Y., Xu, Z., Li, J. Y., Mao, S. & Wang, H. Graphene-Assisted Electron-Based Imaging of Individual Organic and Biological Macromolecules: Structure and Transient Dynamics. *ACS Nano* **19**, 120-151 (2025).

28 Lee, C., Wei, X. D., Kysar, J. W. & Hone, J. Measurement of the elastic properties and intrinsic strength of monolayer graphene. *Science* **321**, 385-388 (2008).

29 Bunch, J. S. *et al.* Impermeable atomic membranes from graphene sheets. *Nano Lett.* **8**, 2458-2462 (2008).

30 Sun, P. Z. *et al.* Unexpected catalytic activity of nanorippled graphene. *Proc. Natl. Acad. Sci. U.S.A.* **120**, e230048112010 (2023).

31 Budrikis, Z. & Zapperi, S. Temperature-Dependent Adhesion of Graphene Suspended on a Trench. *Nano Lett.*

16, 387-391 (2016).

32 Eugen Ermantraut, K. W., Willem Tichelaar. Perforated support foils with pre-defined hole size shape and arrangement. *Ultramicroscopy* **74**, 75-81 (1998).

33 Noble, A. J. *et al.* Routine single particle cryoEM sample and grid characterization by tomography. *Elife* **7**, e34257 (2018).

34 Zheng, L. M. *et al.* Self-assembled superstructure alleviates air-water interface effect in cryo-EM. *Nat. Commun.* **15**, 7300 (2024).

35 Naydenova, K., Jia, P. P. & Russo, C. J. Cryo-EM with sub-1 Å specimen movement. *Science* **370**, 223-226 (2020).

36 Zhang, Q. *et al.* Atomic dynamics of electrified solid-liquid interfaces in liquid-cell TEM. *Nature* **630**, 643-647 (2024).

37 Clark, N. *et al.* Tracking single adatoms in liquid in a transmission electron microscope. *Nature* **609**, 942-947 (2022).

38 Papasergi-Scott, M. M. *et al.* Time-resolved cryo-EM of G-protein activation by a GPCR. *Nature* **629**, 1182-1191 (2024).

39 Klebl, D. P. *et al.* Swinging lever mechanism of myosin directly shown by time-resolved cryo-EM. *Nature* **642**, 519-526 (2025).

40 Bhardwaj, A. *et al.* Fabrication of angstrom-scale two-dimensional channels for mass transport. *Nat. Protoc.* **19**, 240-280 (2024).

41 Chen, B. *et al.* Edge-feeding synchronous epitaxy of layer-controlled graphene films on heterogeneous catalytic substrates. *Nat. Commun.* **16**, 5490 (2025).

42 Cheng, H. *et al.* Dual-Affinity Graphene Sheets for High-Resolution Cryo-Electron Microscopy. *J. Am. Chem. Soc.* **145**, 8073-8081 (2023).

43 Qu, G. *et al.* Structure of a group II intron in complex with its reverse transcriptase. *Nat. Struct. Mol. Biol.* **23**, 549-557 (2016).

44 Mastronarde, D. N. Automated electron microscope tomography using robust prediction of specimen movements. *J. Struct. Biol.* **152**, 36-51 (2005).

45 Lei, J. & Frank, J. Automated acquisition of cryo-electron micrographs for single particle reconstruction on an FEI Tecnai electron microscope. *J. Struct. Biol.* **150**, 69-80 (2005).

46 Zheng, S. Q. *et al.* MotionCor2: anisotropic correction of beam-induced motion for improved cryo-electron microscopy. *Nat. Methods* **14**, 331-332 (2017).

47 Punjani, A., Rubinstein, J. L., Fleet, D. J. & Brubaker, M. A. cryoSPARC: algorithms for rapid unsupervised cryo-EM structure determination. *Nat. Methods* **14**, 290-296 (2017).

48 Pettersen, E. F. *et al.* UCSF Chimera--a visualization system for exploratory research and analysis. *J. Comput. Chem.* **25**, 1605-1612 (2004).

49 Yang, Z. *et al.* Electrospray-assisted cryo-EM sample preparation to mitigate interfacial effects. *Nat. Methods* **21**, 1023-1032 (2024).

50 Eisenstein, F. *et al.* Parallel cryo electron tomography on in situ lamellae. *Nat. Methods* **20**, 131-138 (2023).

51 Kremer, J. R., Mastronarde, D. N. & McIntosh, J. R. Computer visualization of three-dimensional image data using IMOD. *J. Struct. Biol.* **116**, 71-76 (1996).

52 Liu, N. *et al.* Bioactive Functionalized Monolayer Graphene for High-Resolution Cryo-Electron Microscopy.

J. Am. Chem. Soc. **141**, 4016-4025 (2019).

Methods

Preparing uniform holes with industry-compatible lithography

Substrate: Before performing lithography, a 100-nm-thick Cu film was deposited by magnetron sputtering onto a 6-inch silicon wafer to act as the substrate. Deposition occurred at a basal pressure of ~0.08 Pa and a radio frequency power of ~100 W.

Lithography: To ensure exposure precision, a 90-nm-thick BARC (Bottom Anti-Reflective Coating, AR3-600) layer was first spun onto the Cu film/silicon wafer and baked at 180 °C for 1 min. Next, a 460-nm-thick positive photoresist (UV135G, Dow) was spin-coated and soft-baked at 120 °C for 1 min. The wafer was then exposed to 248 nm deep ultraviolet (DUV) light in a lithography tool (Canon, 3030ex6) to transfer the pre-designed hole patterns from the mask to the photoresist. A post-exposure bake (PEB) at 130 °C for 1 min followed, inducing a solubility change in the exposed regions. Finally, the hole patterns were obtained by selectively dissolving the exposed photoresist using a development process. Note that, this industry-compatible lithography process can be readily implemented in standard semiconductor foundry platforms.

Fabricating holey carbon grids

Etching: To release the holey photoresist film from the silicon wafer substrate, both the BARC layer and Cu film were selectively etched. The BARC layer was removed via O_2 reactive ion etching at 200 W for 50 s. The wafer was then immersed in a 1 M $(NH_4)_2S_2O_8$ aqueous solution to dissolve the Cu film. After etching, the holey photoresist film detached from the wafer and floated on the etchant solution. It was subsequently transferred onto the deionized water surface to remove away residual etchant (Fig. S2).

Transfer: The transfer process involved: (1) immersing a filter paper in deionized water, (2) positioning metal grids (e.g., Au 300 mesh) on the submerged paper, then (3) depositing the holey photoresist film onto the metal grids by gradually siphoning off the water. Finally, these grids were air-dried to ensure reliable adhesion between holey photoresist film and metal grids.

Carbon Deposition: Using the holey photoresist film as a template, we successfully replicated its morphology by depositing a 30-nm-thick carbon film onto the photoresist-coated grids via pulsed-current sputtering (40-70 A, Quorum Q160T ES), thus fabricating a holey carbon film with identical pore architecture.

Rinsing and drying: The grids were submerged in acetone to remove the photoresist template and then transferred into isopropanol (IPA) for further rinsing. After drying, the homemade holey carbon grids were obtained.

Graphene transfer for preparing graphene reservoirs

Graphene raw materials: The monolayer and tri-layer graphene films grown on the copper foils were purchased from Beijing Graphene Institute (BGI). The tri-layer graphene films, synthesized via the synchronous growth method[41], exhibited exceptional layer homogeneity, nearly 100% Bernal stacking, and superior mechanical properties.

Graphene transfer: The graphene films were transferred onto the homemade holey carbon grids using a polymer-free transfer method[34]. Firstly, the stearic acid solution (0.005 wt%, dissolved in IPA) was dropped onto the graphene surface. After the evaporation of IPA, self-assembled monolayer of stearic acid spontaneously formed on the graphene. The self-assembled monolayers could maintain the intactness of free-standing graphene on the etchant solution after the copper foil was etched off, thus circumventing the use of polymer in conventional transfer methods. Subsequently, homemade holey carbon grids were carefully placed onto the surface of free-standing graphene. The vdW interactions between graphene membrane and holey carbon film ensured the reliable adhesion, contributing to the high-coverage graphene reservoirs.

Rinsing and drying: The graphene grids were transferred onto the deionized water surface to remove away the residual etchant, followed by rinsing in IPA for 2-5 min to eliminate the stearic acid molecules. After being taken out from the IPA, the graphene grids were air-dried.

We note that the fabrication procedures for conventional graphene grids are nearly identical to those for graphene reservoir grids, differing only in the type of grid used. Conventional graphene grids were prepared using the commonly-used commercially available grids (Quantifoil-R1.2/1.3).

AFM, SEM and STEM characterizations

The morphologies of graphene reservoirs were characterized by atomic force microscopy (AFM, Bruker Dimension Icon equipped with Nanoscope V controller) in tapping mode using a commercially available AFM tip (OTESPA-R3, Bruker). The coverage of graphene reservoir grid was collected using scanning electron microscopy (SEM) (2 kV, Hitachi S-4800), and the aberration-corrected scanning transmission electron microscopy (STEM) images of graphene were carried out using a Nion U-HERMS200 microscope at 60 kV.

Preparation of biological samples

The 20S proteasome was expressed and purified from *Escherichia coli* cells by following previous established methods[42], and diluted to 0.3 mg/mL for use. The Ll.LtrB group II intron was purified by following previously established methods[43], and diluted to 0.4 μM for use. Apoferritin was purchased from Sigma-Aldrich (Catalog: A3660) and diluted to 1 mg/mL for use. Streptavidin was purchased from NEB (Catalog: N7021S) and diluted to 0.1 mg/mL for use. The SARS-CoV-2

spike protein was kindly provided by Dr. Qiang Zhou at Westlake University and diluted to 0.4 mg/mL for use.

Cryo-EM specimen preparation using graphene reservoirs

For cryo-EM specimens used to demonstrate ice thickness control, a 3 μL sample solution was pipetted onto the monolayer graphene reservoir grid (Au 300 mesh, 1200 nm hole diameter), which had been glow-discharged in a plasma cleaner machine (Harrick Plasma) for 15~30 s at a low power setting. The grid was transferred into a Vitrobot Mark IV (Thermo Fisher Scientific) with the chamber temperature set to 8 °C and humidity maintained at 100%. The blotting force was set to -2, the waiting time to 10 s, and different blot times (2 s, 6 s, 8 s, 10 s, and 12 s) were tested. The grids were then plunge-frozen in liquid ethane and stored in liquid nitrogen for subsequent cryo-EM imaging.

For monolayer graphene reservoir grids with varying hole diameters, the Vitrobot blotting time are as following: 5-6 s for 600 nm, 7-8 s for 800 nm, 8-10 s for 1200 nm, and 12-13 s for 2000 nm diameters. All other parameters remained as described previously. For structural determination of the *Ll.LtrB* group II intron, we used a monolayer graphene reservoir grid (Au 300 mesh, 1200 nm hole diameter) with a blotting time of 10 s, maintaining all other parameters as previously described.

Fabrication of cryo-EM samples embedded in graphene reservoir sandwiches

Preparation of top graphene for sandwich structure:

(1) We used the trilayer graphene as the top layer of sandwich structure. The commercially available trilayer graphene (Beijing Graphene Institute) was grown on the copper foil. To remove the graphene on the backside of copper foil, the foil was put into a reactive ion etcher (Pico SLS, Diener) with an air flow of 5 sccm. The air plasma was then generated at a controlled power of 150W. After a 3-minute treatment, the graphene on the backside was completely removed, while the trilayer graphene on the opposite side of the copper foil remained intact.

(2) The trilayer graphene/copper foil was placed on the surface of 1 M $(NH_4)_2S_2O_8$ aqueous solution to etch the Cu foil. After etching, the freestanding trilayer graphene remained floating on the etchant solution surface. Notably, a self-assembled monolayer of stearic acid could be used to increase the robustness of freestanding trilayer graphene if needed. The fabrication procedures for the self-assembled monolayers were detailed in the “Graphene transfer for preparing graphene reservoirs” section.

(3) The freestanding trilayer graphene was carefully transferred from the etchant solution onto the surface of deionized water using a sieve mesh. This transfer process onto fresh deionized water was repeated twice to ensure the removal of residual etchant. Subsequently, the freestanding trilayer graphene was transferred onto the surface of the buffer solution.

Preparation of bottom graphene for sandwich structure:

(4) A 3 μL sample solution was pipetted onto the monolayer graphene reservoir grid (Au 300 mesh, 1200 nm hole diameter), which had been glow-discharged in a plasma cleaner machine (Harrick Plasma) for 30 s at a low power setting.

(5) Then the sample-loaded grid was immediately immersed beneath the free-standing trilayer graphene film and then the film was scooped up rapidly.

Blotting and plunge-freezing:

(6) The graphene reservoir sandwich grid was transferred into a Vitrobot Mark IV (ThermoFisher Scientific), and the temperature of the Vitrobot chamber was set as 8 °C with a humidity of 100%. The blotting force was set to -1, the waiting time was set to 10 s, and the blotting time was set to 20-22 s.

(7) The grid was subsequently plunged into liquid ethane and stored in liquid nitrogen for further cryo-EM imaging.

For the trilayer graphene reservoir grids, all the parameters were kept the same.

Conventional cryo-EM specimen preparation

Conventional graphene grids (Quantifoil, Au 300 mesh, R1.2/1.3) featuring protruding holes served as controls. For cryo-EM specimen preparation, apoferritin samples (3 μL) were applied to these grids using a 10 s blot time, with all other parameters consistent with graphene reservoir protocols.

For conventional graphene sandwiched sample, a 3 μL sample solution was pipetted onto the conventional graphene grid, which had been glow-discharged in a plasma cleaner machine (Harrick Plasma) for 30 s at a low power setting. Then the sample-loaded grid was also immediately immersed beneath the freestanding trilayer graphene film and then scooped the film up rapidly. Next, the conventional graphene sandwich grid was positioned on the filter paper (Ted Pella, 47000-100), which was used to remove excess solution from the sandwiched area. Finally, the manually-blotting grid was plunged into liquid ethane and stored in liquid nitrogen for further cryo-EM imaging.

Cryo-EM data collection and structural analysis

The single-particle Cryo-EM dataset of graphene reservoir for Ll.LtrB group II intron was automatically collected using EPU software on a Thermo Fisher Scientific Titan Krios G3i TEM (300 kV), equipped with a GIF-Quantum energy filter (20 eV) and a Gatan K3 direct electron detector. A Total of 6,528 micrographs were collected with a pixel size of 0.83 Å. For the dataset of conventional graphene sandwich grid and graphene reservoir sandwich grid for motion analysis, 180 and 103 micrographs were automatically collected, respectively, with a pixel size of 0.97 Å,

using SerialEM software[44] on an FEI Titan Krios TEM (300 kV) equipped with a Gatan K3 direct electron detector. For the dataset of graphene reservoir sandwich grid for SARS-CoV-2 spike protein and streptavidin, 4,377 micrographs with a pixel size of 0.8374 Å, and 3,646 micrographs with a pixel size of 0.5141 Å were automatically collected, respectively, using AutoEMation software[45] on a Thermo Fisher Scientific Titan Krios TEM (300 kV) equipped with a Gatan K3 direct electron detector and a GIF-Quantum energy filter (20 eV). For the dataset of graphene reservoir grid and conventional graphene grid for apoferritin, 178 and 304 micrographs with a pixel size of 0.836 Å were automatically collected using SerialEM software on an FEI Tecnai Arctica TEM (200kV) equipped with a Gatan K2 camera.

All the micrographs aforementioned were fractioned to 32 frames with a summed electron dose of 50 $e^{-}/Å^2$ and motion-corrected by MotionCor2[46]. Then the motion-corrected micrographs were imported into CryoSPARC[47] for patch CTF estimation, micrograph selection, particle picking, 2D classification, hetero refinement and the final 3D reconstruction (Figures S20, and S22). The number of particles used for the final 3D reconstruction of graphene reservoir grid for Ll.LtrB group II intron, graphene reservoir sandwich grid for SARS-CoV-2 spike protein and streptavidin were 179,409, 150,268, and 154,497, respectively. The reported resolutions were 2.70 Å, 2.88 Å, and 2.69 Å, respectively, determined using Fourier shell correlation (FSC) = 0.143 as the cut-off criterion. PDB 5G2X (https://www.rcsb.org/structure/5G2X), 8HRI (https://www.rcsb.org/structure/8HRI), and 8HRM (https://www.rcsb.org/structure/8HRM) were used to dock into the density maps of Ll.LtrB group II intron (EMD-66426), SARS-CoV-2 spike protein (EMD-66423), and streptavidin (EMD-66424), and all the structure details were visualized using Chimera[48]. The Euler angles for each particle in the final particle dataset of Ll.LtrB group II intron, SARS-CoV-2 spike protein, and streptavidin were plotted for the orientational distribution analysis.

To analyze the spatial distribution of protein particles in confined ice, local CTF refinement in CryoSPARC was performed to estimate the local defocus values of individual apoferritin particles from graphene reservoir grid, and subsequently to plot the three-dimensional graphics according to their *x, y,* and *z* coordinates, showing the spatial distribution of inclined planes relative to the *xy* plane. For the detailed processing pipeline, refer to previously established methods[49].

In our particle utilization analysis comparing conventional graphene grids with graphene reservoir grids (10 s blotting time), we initially selected 89,151 and 34,407 raw particles, respectively. Following refinement, 33,900 (38.0% utilization) and 24,028 (69.8% utilization) particles remained for final 3D reconstruction.

To measure particle motion as a function of accumulated electron dose in both confined and non-confined ice, Bayesian polishing in Relion 3.0.8 was used to determine the particle coordinates in each frame, which were then used to calculate the root-mean-squared displacements of per particle and plotted versus electron dose. For both samples, three particle-motion measurements were performed, and each of them was based on thousands of particles.

Cyro-ET data collection and analysis

The cryo-ET data were collected with tilt angles ranging from +60° to −60° at 3° intervals, using SerialEM software equipped with PACETomo[50] on a Thermo Fisher Scientific Titan Krios TEM (300 kV) equipped with a Gatan K3 direct electron detector and a GIF-Quantum energy filter (20 eV), or using SerialEM software on an FEI Titan Krios TEM (300 kV) equipped with a Gatan K3 direct electron detector. The pixel sizes were 0.8697 Å (graphene reservoir grid with 600 nm hole), 1.642 Å (graphene reservoir grids with 800 nm, 1200 nm, and 2000 nm holes), and 1.25 Å (graphene sandwich grid). Each tilt was fractionated into 8 frames with a cumulative dose of 3 $e^{-}/Å^2$ per tilt, resulting in a total dose of 120 $e^{-}/Å^2$ for the complete tilt series. The tilt series were firstly motion-corrected using MotionCor2 and then imported into IMOD[51] for further alignment and tomogram reconstruction. The final tomograms were generated with a binning factor of 4. The position of 20 proteasome particles in graphene reservoir sandwiched sample was manually identified and plotted[52].

Data availability

The cryo-EM density maps of Ll.LtrB group II intron, SARS-CoV-2 spike protein and streptavidin have been deposited into EMDB under the accession numbers of EMD-66426, EMD-66423, and EMD-66424, respectively. Any additional data supporting the findings in this manuscript are available from the corresponding authors upon reasonable request.

Acknowledgments

Liming Zheng thanks Prof. Sir Andre Geim for his inspiring works in 2D materials and confined liquid. We gratefully acknowledge the Electron Microscopy Laboratory and Molecular Materials and Nanofabrication Laboratory (MMNL) in the College of Chemistry at Peking University for providing instrument access. The work is supported by the funding from the National Key Research and Development Program of China (Grant 2024YFA1307301 to H.-W.W.), National Natural Science Foundation of China (31825009 to H.-W.W.; 52021006, T2188101 to H.L.P.; 22402007 to L.M.Z.; 12325202 to X.D.W.; 12432003 to Z.H.D.), Beijing National Laboratory for Molecular Sciences (BNLMS-CXTD-202001), THE XPLORER PRIZE (to H.-W.W. and H.L.P.) and The University of Hong Kong's Seed Fund to N. L.

Competing interests

The authors, Hailin Peng, Liming Zheng and Xiaole Zhao, and have filed the Chinese patent applications (ZL202410883073.3), covering the procedures of preparing TEM grids for fabricating graphene reservoirs.

Author contributions

L.Z., H.-W.W., and H. P. conceived the idea. L.Z. and X.Z. prepared the graphene reservoir grids. J.S., N.L., J.X., Z.W., J.Y. and Y.X. carried out the cryo-EM characterizations. N.L., J.S., L.Z., and H.-W.W. analyzed the cryo-EM data. J.C., L.Z., Z.D. and X.W. performed theoretical simulations and mechanical analyses. X.Z., L.Z., X.G. and W.S. carried out the characterizations of graphene reservoirs. L.Z. and H.L. contributed to the lithography. B.C. and L.S. synthesized graphene film. L.Z., N. L., H.P., and H.-W.W. wrote the manuscript with the contributions from J.S., X.Z., J.C., Z.D. and X.W. All authors discussed the results and gave approval to the final version of the manuscript.

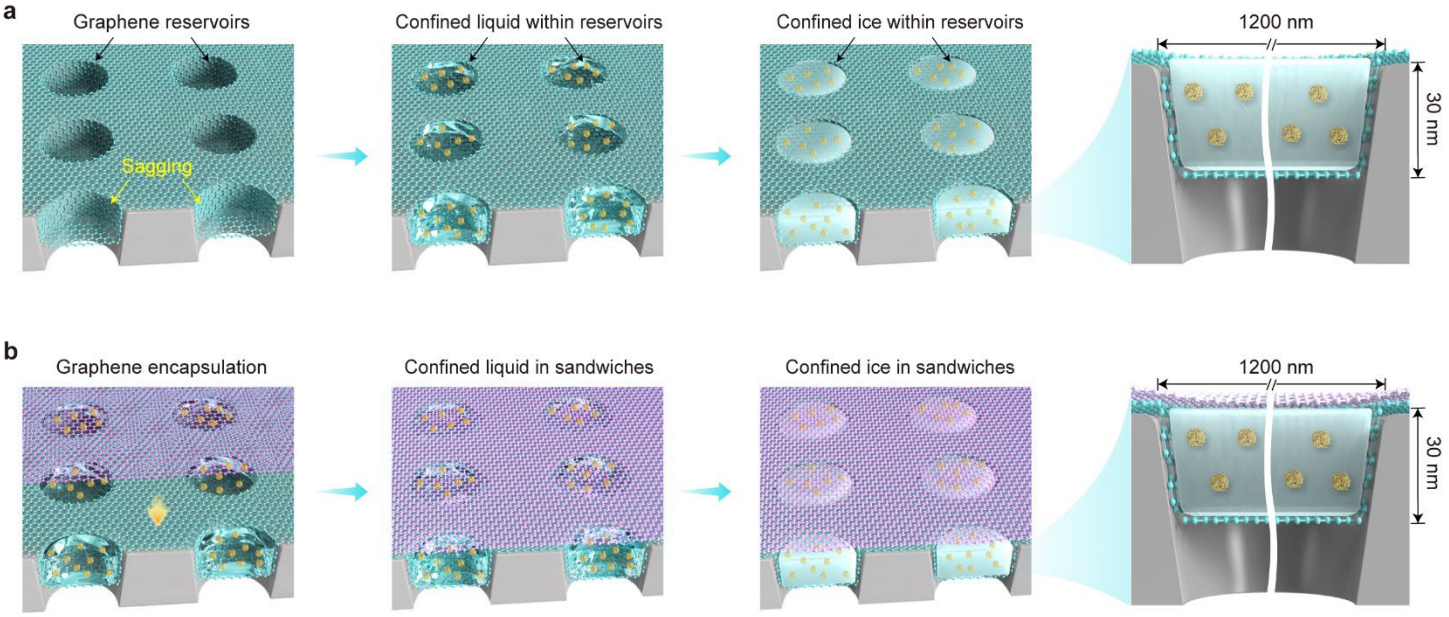

Fig. 1 | Schematic illustration of controlling ice thickness in cryo-EM via confinement. a, The adhesion of suspended graphene to the hole sidewall causes the sagging morphology of graphene, forming graphene reservoirs for liquid confinement. After plunge-freezing, uniform vitreous ice layers are prepared with controllable thickness by adjusting the depth of graphene reservoirs. To convey the size correlation between hole diameter and reservoir depth, the right panel employs a white interval to indicate the representative dimensions. **b,** The liquid is encapsulated by depositing an additional graphene sheet onto the surface of graphene reservoirs, forming confined liquid films in the graphene sandwich structures. Subsequent plunge-freezing yields uniform confined ice with precisely controlled thickness.

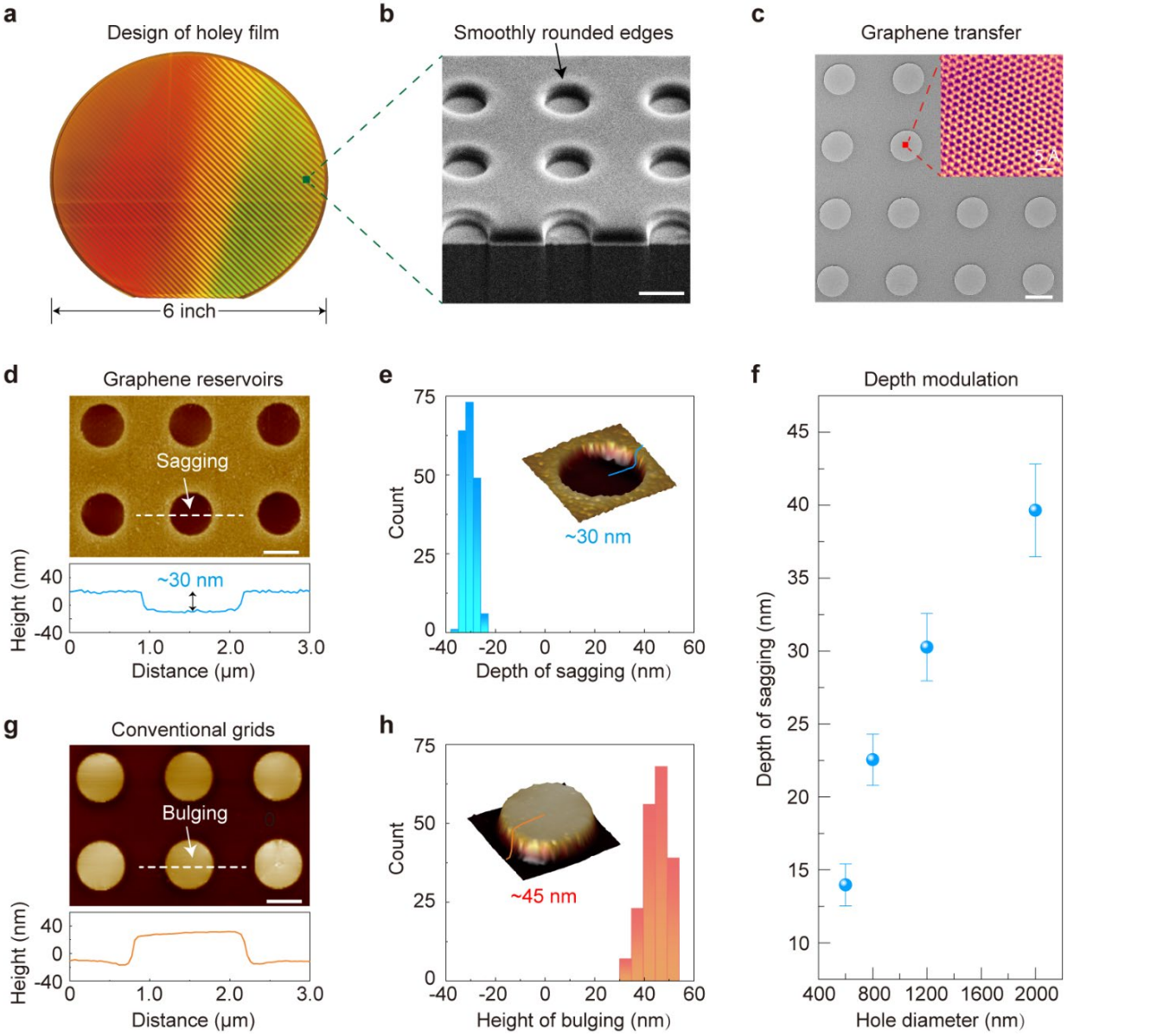

Fig. 2 | Scalable fabrication and depth modulation of graphene reservoirs. a, Optical image showing a 6-inch wafer with high-density hole arrays fabricated by industry-compatible lithography. **b,** Magnified cross-sectional SEM image from (a), showing the smoothly rounded edges of the holes. **c,** Suspended graphene membranes transferred onto holes of home-made TEM grid. Inset: atomic-resolution imaging of graphene lattice. **d,** Representative AFM image reveals that suspended graphene membranes over the holes exhibit a sagging morphology, with a depth of ~30 nm measured from the depth profile, forming graphene reservoirs. **e,** Sagging depth distribution of graphene reservoirs (centered at 30 nm). Inset: 3D sagging morphology of graphene reservoir characterized by AFM. **f,** Tunable depth of graphene reservoirs (14~40 nm) achieved through hole diameter control. **g,** Typical AFM image shows that suspended graphene membranes over conventional grid holes exhibit a bulging morphology, with a height of ~45 nm measured from the height profile. **h,** Bulging height distribution of conventional grids (average: 45 nm). Inset: 3D bulging morphology of conventional grid characterized by AFM. Scale bars, 1 μm.

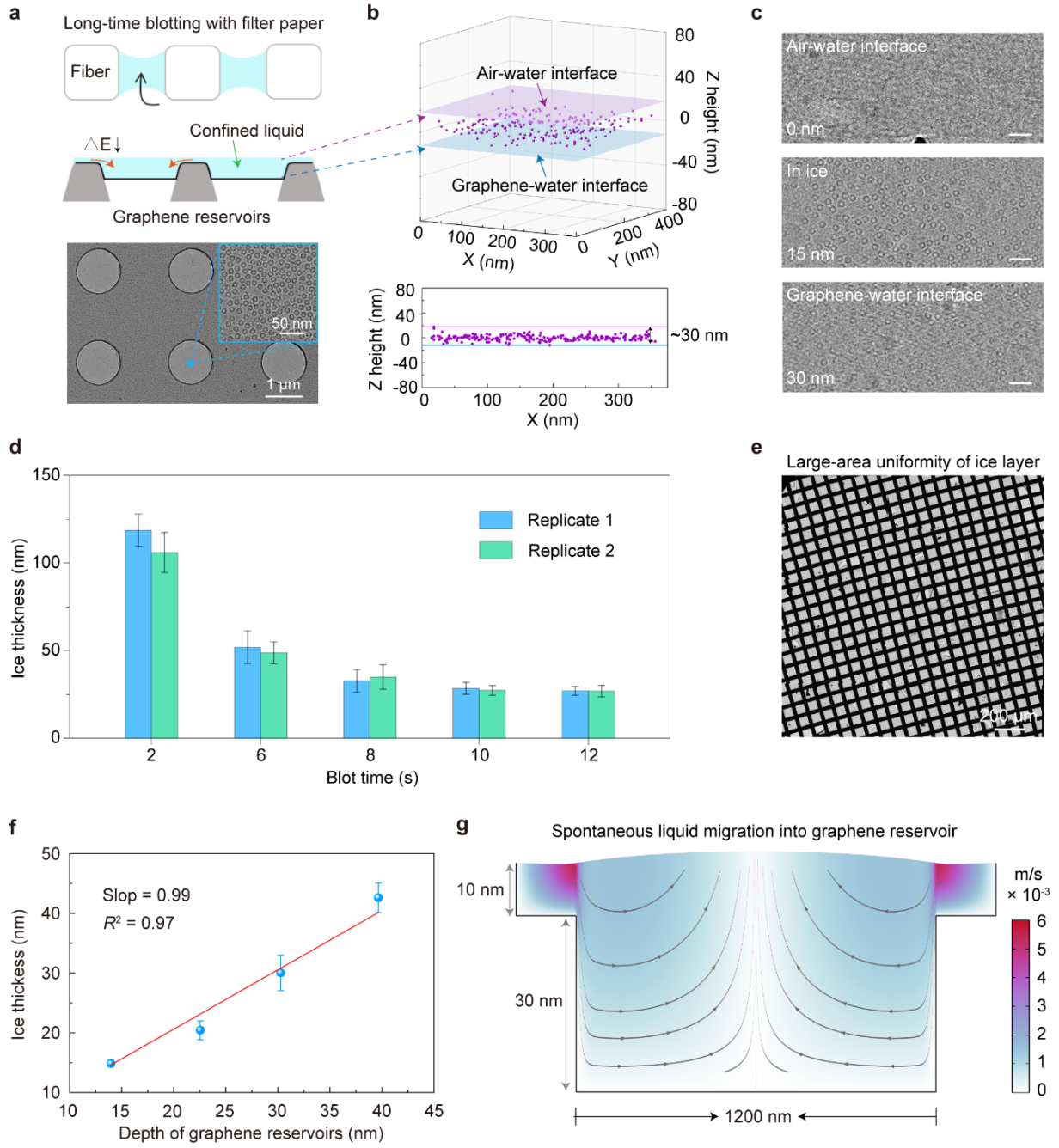

Fig. 3 | Precise control of ice thickness using graphene reservoirs. a, Top: schematic shows that confined liquid film in graphene reservoirs remains stable after a long time (10s) blotting. Bottom: typical cryo-EM image showing protein particles embedded in the confined vitreous ice. **b,** Spatial distribution of protein particles within the confined ice layer. Top: 3D perspective; Bottom: 2D perspective. Each purple spot represents one individual protein particle. **c,** Typical cryo-ET slices extracted from the cryo-ET reconstruction of the cryo-specimen showing the air–water interface (top), in-ice layer (middle), and graphene–water interface (bottom), respectively. Scale bars, 50 nm. **d,** Statistical analysis of ice thickness generated with different blotting times. At longer blotting times (8-12 s), the ice thickness corresponds with the depth of the graphene reservoirs (~30 nm). The results are comparable in two replicate experiments, demonstrating reliable reproducibility. Each replicate constitutes of several grids. **e,** Typical overview atlas of the cryo-specimen showing the large-area uniformity of ice layer. **f,** Tunable ice thickness by controlling the depth of graphene reservoirs. **g,** Numerical simulation reveals spontaneous liquid migration into graphene reservoir from thin peripheral regions. The colors denote differences in flow velocity, while the arrows show the flow direction.

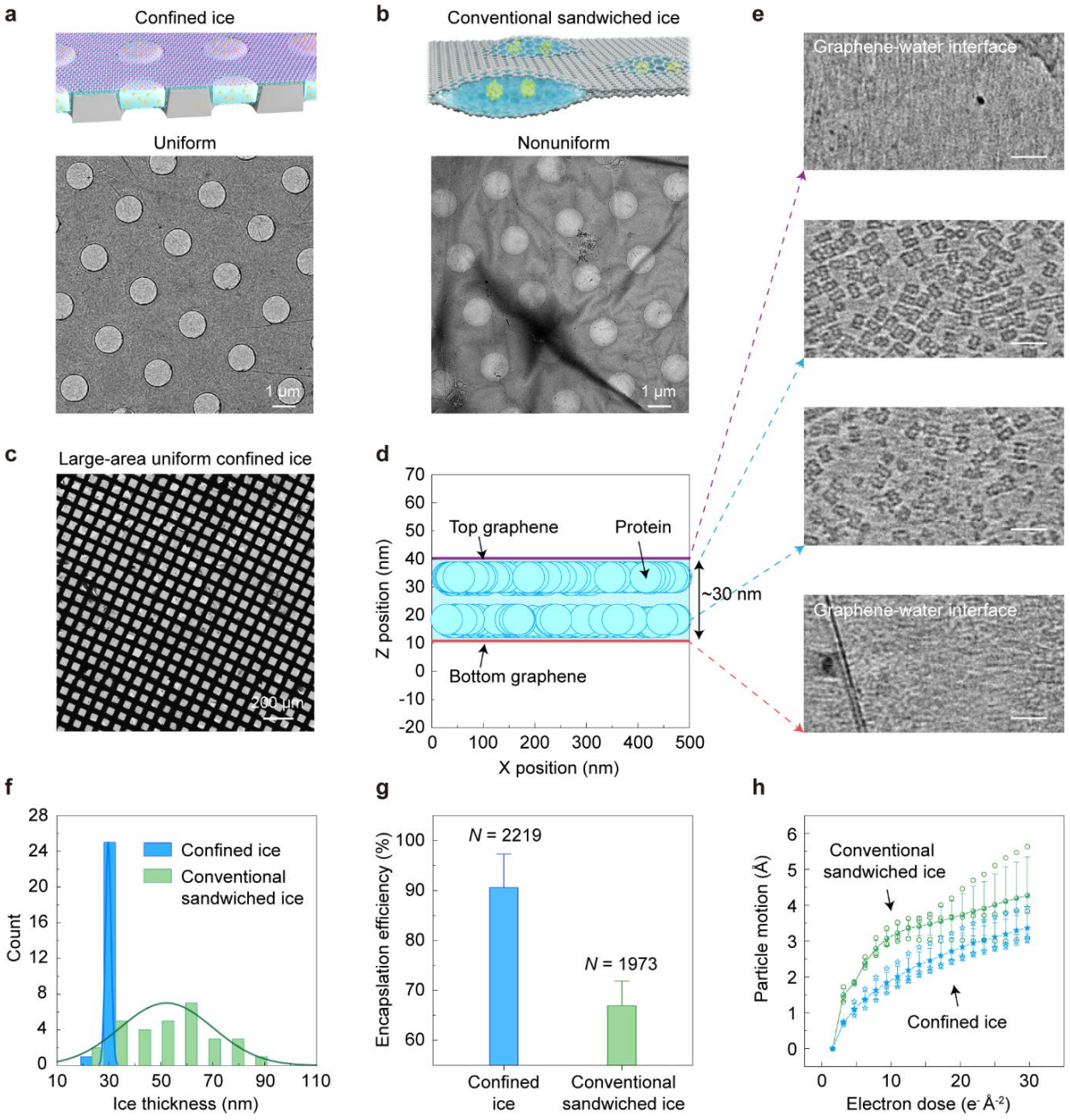

Fig. 4 | Uniform confined ice in graphene reservoir sandwich with controllable thickness. a-b, Schematic illustrations and corresponding cryo-EM images showing uniform confined ice in graphene reservoir sandwich (a), and heterogeneous ice thickness for conventional sandwiched ice (b), respectively. **c,** Typical overview atlas of grid showing the large-area uniformity of confined ice. **d,** Cryo-ET reconstruction reveals the thickness of confined ice (~30 nm) and the spatial distribution of embedded protein particles. Each blue circle represents an individual 20S proteasome particle. **e,** Representative cryo-ET slices extracted from (d) showing the top graphene–water interface, in-ice layer, and bottom graphene–water interface, respectively. **f,** Comparative ice thickness statistics: confined ice in graphene reservoir sandwich (blue) displays a narrow peak at 30 nm, whereas conventional sandwiched ice (green) exhibits a broader distribution (52 ± 17 nm). **g,** Encapsulation efficiency comparison: confined ice in graphene reservoir sandwich achieves >90% success rate (N = 2,219 grid squares) versus conventional sandwiched ice at ~67% (N = 1,973 grid squares). **h,** Particle motion with accumulated electron dose in confined ice (blue) and conventional sandwiched ice (green). Each dotted line represents the motion average of thousands of individual particles, while the solid lines are the average of these dotted lines.

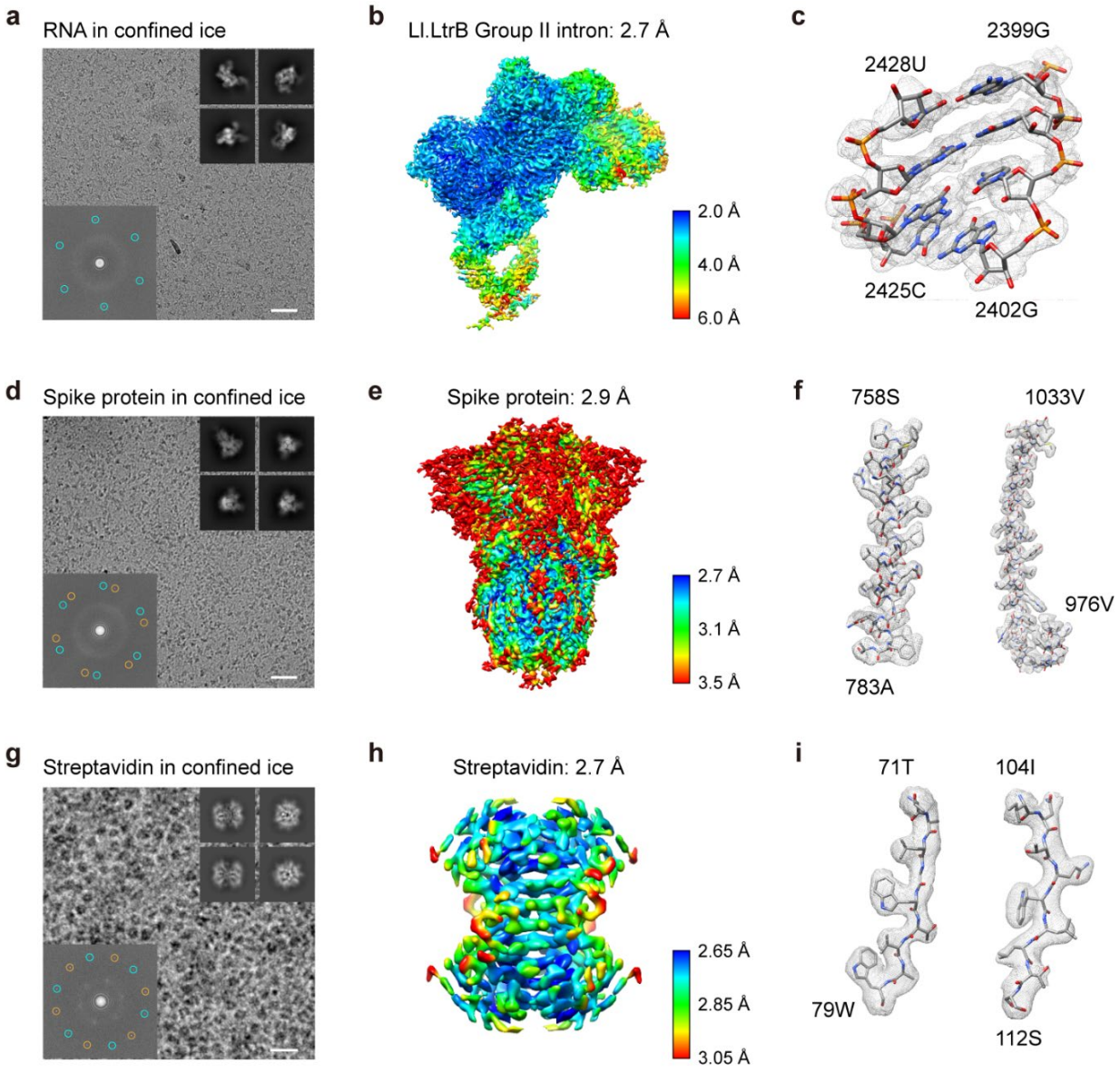

Fig. 5 | Uniform confined ice enabled high-resolution cryo-EM reconstructions. a, d, g, Representative cryo-EM images of RNA (Ll.LtrB Group II intron) in graphene reservoirs (**a**), spike protein in graphene reservoir sandwiches (**d**) and streptavidin in graphene reservoir sandwiches (**g**), respectively. Insets: typical 2D class averages (upper-right) and Fourier transform of the cryo-EM image (bottom-left). The hexagonal diffraction spot patterns exhibit a twist angle in (d) and (g), indicating the coexistence of top and bottom graphene layers in the sandwich structure. **b, e, h,** The 3D density maps of Ll.LtrB Group II intron at 2.7 Å resolution (**b**), spike protein at 2.9 Å resolution (**e**), and streptavidin at 2.7 Å resolution (**h**), respectively. These maps are colored to visualize the local resolution distribution. **c, f, i,** Selected densities from the Ll.LtrB Group II intron map (**c**), spike protein map (**f**), streptavidin map (**i**) with the corresponding atomic models docked.